**Article ID:** 1000-324X(2020)05-0608-09 **DOI:** 10.15541/jim20190276

# Hollow Carbon Sphere with Tunable Structure by Encapsulation Pyrolysis Synchronous Deposition for Cefalexin Adsorption

DU Juan, LIU Lei, YU Yifeng, ZHANG Yue, LÜ Haijun, CHEN Aibing

(College of Chemical and Pharmaceutical Engineering, Hebei University of Science and Technology, Shijiazhuang 050018, China)

**Abstract:** Hollow carbon spheres (HCS) with controllable diameter and shell thickness using a simple encapsulation pyrolysis synchronous deposition method is reported. This method changed the polystyrene spheres (PS), a widely used sacrifice hard template, into carbon by a pyrolysis and synchronous deposition process in the hermetical silica shell, without any cross-linking agent and catalyst, simplifying synthesis, and lowering costs. The obtained HCS exhibited uniform spherical morphology with tailorable particle size (190–1600 nm) and well controlled hollow voids. Moreover, HCS samples with precisely tuned thickness (4.5–13.5 nm) were obtained only by changing the silica precursor amount. The resultant HCS showed promising potential for applications in cefalexin adsorption with capacity of 291 $mg \cdot g^{-1}$. Therefore, this synthetic strategy may offer an efficient production route to commercial applications for HCS.

**Key words:** hollow carbon spheres; encapsulation pyrolysis synchronous deposition; tunable structure; cefalexin adsorption

Hollow carbon spheres (HCS) continue to be a research focus due to their unique properties such as high surface-to-volume ratios, and excellent chemical and thermal stabilities[1-3] with diverse applications in the field of adsorption, drug delivery, catalysis, nano-devices, and energy storage/conversion[4-5]. The application of HCS relies strongly on their structural properties, such as controlled diameter and shell thickness, surface properties, crystallinity of the carbon shell, and porous structure on shell[4, 6]. Numerous methods have been explored for the synthesis of adjustable HCS, including nanocasting method, soft template method or chemical vapor deposition strategy. The nanocasting method highlights a nanocasting procedure by depositing a suitable carbon precursor onto the removable seeds and therefore being widely adopted due to the precise control on the structure[7]. In general, the nanocasting method usually starts from constructing a core/shell structure with sacrificial hard templates (e. g. polymer or $SiO_2$ nanoparticles) as core materials, which are coated with carbon sources such as polymers.

Polystyrene spheres (PS), a typical polymer, are often used as self-sacrifice hard template for hollow sphere due to its easy removal through changing into waste organic gases. Meanwhile, it can also be used as a promising carbon precursor due to high carbon content, facile preparation and adjustable diameter. Therefore, it is facilitate to prepare hollow carbon nanostructures by using PS spheres as carbon sources directly.

Generally, crosslinking or metal catalysis enable it to transform into carbon materials. Some methods (*e. g.* Friedel-Crafts reaction) was used for preparation of functional carbon materials using PS as carbon precursor[8-9]. In our previous work, we had fabricated controllable hollow carbon spheres by dissolution-capture method using PS as carbon sources[9-10]. However, based on this method, it is hard to control core/shell size and unsuitable for large scale preparation. Moreover, it is necessary to introduce metal to ensure the spherical morphology[11]. There is a great need to prepare highly uniform, monodispersed high-quality HCS materials with tunable particle size and adjustable shell thickness by a simple method.

Herein, we reported a novel synthesis of HCS with tailorable nano-size and shell thickness using an encapsulation pyrolysis synchronous deposition. The key to this approach was to encapsulate the easily decomposed PS in a compact silica shell. Thermal decomposable polymer nanosphere (PN) was encapsulated in compact silica shell and then transform into volatile carbonaceous

**Received date:** 2019-06-06; **Revised date:** 2019-08-31
**Foundation item:** National Natural Science Foundation of China (21676070)
**Biography:** DU Juan(1992–), female, PhD candidate. E-mail: dujuan_chemistry@163.com
杜鹃(1992–), 女, 博士研究生. E-mail: dujuan_chemistry@163.com
**Corresponding author:** CHEN Aibing, Professor. E-mail: chen_ab@163.com
陈爱兵, 教授. E-mail: chen_ab@163.com

species which deposited on the HCS to form a carbon layer, instead of the common process of crosslinking or metal catalysis. The diameter size of the HCS could be tunable by simple adjusting the size of PS core. Moreover, HCS with different thickness of carbon shell were also obtained through simply changing the amount of TEOS, facile and efficient for the synthesis of well-defined HCS, which may provide a potential platform for treatment of antibiotic wastewater.

# 1 Experimental

## 1.1 Synthesis of PS nanoparticles

PS nanoparticles with different diameter size were prepared by following the previous methods with slight modification [6]. Typical synthesis of 200 nm PS spheres were performed under argon. Briefly, 94 μL oleic acid and 1.75 mL styrene were dissolved in 141 mL water, and then stirred at 60 ℃ for 1 h. After addition of 80 mg potassium persulfate, the solution was further heated to 70 ℃ accompanied by vigorous stirring for 5 h. The PS spheres were collected by centrifugation and washed 3 times with water. The 400, 900 and 1600 nm PS were prepared by adjusting the amount of water and rotate speed at 8000 $r \cdot min^{-1}$ for 5 min of reaction.

## 1.2 Preparation of HCS

To prepare polymer/silica nanohybrids (named PS@$SiO_2$) nanoparticles, we dispersed 0.2 mL of as-prepared PS nanoparticles (124 mg) into 100 mL of ethanol solution, including 100 μL of aminopropyl-ethoxysilane (APTES). After vigorously stirring (4 h), 1 mL of TEOS and 2.5 mL of $NH_3$ were then introduced into the above solution accompanying by stirring, and reacted at room temperature. The solution became milky when it reacted overnight. The white color product of PS@$SiO_2$ nanoparticles was collected using centrifugation (9500 $r \cdot min^{-1}$) and rinsed several times with ethanol and dried at 50 ℃ for 10 h. The as-prepared PS@$SiO_2$ nanoparticles were heated at 2 ℃$\cdot min^{-1}$ from room temperature to 800 ℃ and kept at this temperature for 3 h under a nitrogen flow. The pyrolysis product was treated with aqueous HF solution (10wt%) to remove the silica and generate HCS. Under the same reaction conditions for synthesis of PS@$SiO_2$ core-shell spheres to obtained HCS with different shell thickness, the volume of TEOS was 0.5, 1 and 1.5 mL in the synthesis of HCS-0.5, HCS-1 and HCS-1.5, respectively.

## 1.3 Characterization

X-ray diffraction (XRD) patterns were achieved using a Rigaku D/MAX-2500 system with Cu-Kα ($\lambda$=0.15406 nm). Raman measurements were performed on a Jobin-Yvon HR800 Spectrometer using a 532 nm laser. The morphology and microstructure of HCS samples were investigated by a scanning electron microscopy (SEM, HITACHI S-4800-I) and a transmission electron microscopy (TEM, JEOL JEM-2100). Nitrogen adsorption-desorption isotherms were carried out on a Micromeritics TriStar 3020 instrument at –196 ℃. The Brunauer-Emmett-Teller (BET) method was employed to calculate the specific surface area, while the Barrett-Joyner-Halenda (BJH) method was applied to analyze the pore size distribution using the desorption branch of isotherm. The total pore volume was obtained from amount of $N_2$ adsorbed at the relative pressure ($p/p_0$=0.97). X-ray photoelectron spectroscopy (XPS) was conducted on a Thermo Scientific ESCALab 250Xi system using an Al-Kα radiation under a vacuum of $3\times10^{-8}$ Pa. Thermogravimetric analysis (Pyris 1 TGA) was performed under air flow from 25 ℃ to 800 ℃ at a heating rate of 10 ℃$\cdot min^{-1}$.

## 1.4 Removal of antibiotic from an aqueous solution

Aqueous solution with cefalexin concentration of 0.01 was prepared by dissolving 1 g of cefalexin in 100 mL deionized water. A $4\times10^{-4}$ aqueous cefalexin solution was prepared by further diluting the stock solution with deionized water. The effect of contact time on removal rate of cefalexin with initial concentration of $4\times10^{-4}$ onto different adsorbents was evaluated as follows: 10 mg adsorbent was dried at 50 ℃ overnight, and then dispersed in 100 mL aqueous cefalexin solution ($4\times10^{-4}$). The suspension was then stirred at a constant rate for 1400 min in a sealed vessel at 25 ℃. 500 μL of the cefalexin solution was removed with a syringe-driven filter (pore size of 0.2 μm) from suspension at a pre-determined time, and then diluted to one tenth with water and the concentrations was analyzed using a UV2300 UV-Vis spectrophotometer at the maximum absorbance of 268 nm in order to calculate the cefalexin adsorption capacities. The amount of cefalexin adsorbed was calculated using the equation: $q_t = (C_0 - C_t) \times V/m$, where $C_0$ and $C_t$ are respectively the initial concentration and concentration after $t$ min, $m$ (g) is the mass of adsorbent, and $V$ (L) is the volume of the solution.

To obtain an equilibrium adsorption amount, 10 mg of the adsorbent was added to 100 mL of the cefalexin solution with different initial cefalexin concentrations (25–300 $mg \cdot L^{-1}$) for a certain time until equilibrium was reached. The equilibrium adsorption capacities $q_e$ ($mg \cdot g^{-1}$) were calculated according to the following formula: $q_e = (C_0 - C_e) \times V/m$, where $C_0$ ($mg \cdot L^{-1}$) is the initial concentration of the cefalexin solution, $C_e$ ($mg \cdot L^{-1}$) is the equilibrium concentration of cefalexin, $V$ (L) is the volume of

the solution, and $m$ (g) is the weight of the adsorbent.

### 1.5 Adsorption kinetics

To illustrate the adsorption process, pseudo-first-order kinetic and pseudo-second-order kinetic models were used to fit the experimental data, which can be, respectively, expressed as follows: $\ln(q_e-q_t) = \ln q_e - K_1 t$, $t/q_t = 1/K_2 q_e^2 + t/q_e$, where $q_e$ (mg·g$^{-1}$) and $q_t$ (mg·g$^{-1}$) are the adsorption capacities at equilibrium and at time $t$, and $K_1$ and $K_2$ are the constants of first and second-order adsorption, respectively.

### 1.6 Adsorption isotherms

Langmuir and Freundlich adsorption isothermal models were used to determine the proper isotherm for cefalexin adsorption. The equations of the Langmuir and Freundlich models can be expressed as follows: $C_e/q_e = C_e/q_m + 1/K_L/q_m$, $\ln q_e = \ln K_F + \ln C_e/n$, where $q_m$ (mg·g$^{-1}$) is the maximum adsorption capacity, $C_e$ (mg·L$^{-1}$) is the equilibrium concentration of cefalexin $K_L$ (L·mg$^{-1}$) is the Langmuir constant related to the adsorption energy, and $K_F$ and $n$ are the Freundlich constants and intensity factors, respectively.

## 2 Results and discussion

As illustrated in Fig. 1(a), the formation of HCS derived from PS was achieved in the compact silica shell. Briefly, uniform PS spheres were synthesized by using styrene as the precursor and template, then the PS were uniformly coated by a layer of compact silica. During the pyrolysis process, PS spheres transformed into volatile carbonaceous species and deposited in the hermetical silica shell to form a layer of carbon shell. Route 1 in Fig. 1 illustrates the synthesis of dispersible HCS-1, in which the formation of an inorganic outer compact silica shell was crucial. The outer compact silica shell functions as a nanoreactor to provide a confined nanospace for high temperature pyrolysis of the PS polymer[6]. As a result, the HCS were obtained (black color) after etching the silica shells. By contrast, for the PS coated by mesoporous $SiO_2$, using cetyltrimethyl-ammonium bromide as surfactant[9], there was hardly any carbon residue under pyrolysis and the hollow mesoporous silica spheres were obtained (white color) (Fig. 1(a), route 2). TEM images of PS coated by mesoporous silica (PS@m$SiO_2$) and TEM and SEM images of production mesoporous silica (m$SiO_2$) after pyrolysis was shown in Fig. 1(b, c), which proves the obtained PS coated by mesoporous silica and m$SiO_2$ after pyrolysis.

Morphology and structure of obtained samples were characterized by TEM, which showed that highly uniform and monodisperse nanocomposites are successfully obtained (Fig. 2(a)). Each PS@$SiO_2$ core-shell sphere contains only one PS core at the center. It was apparent that each PS sphere was encapsulated by a silica shell

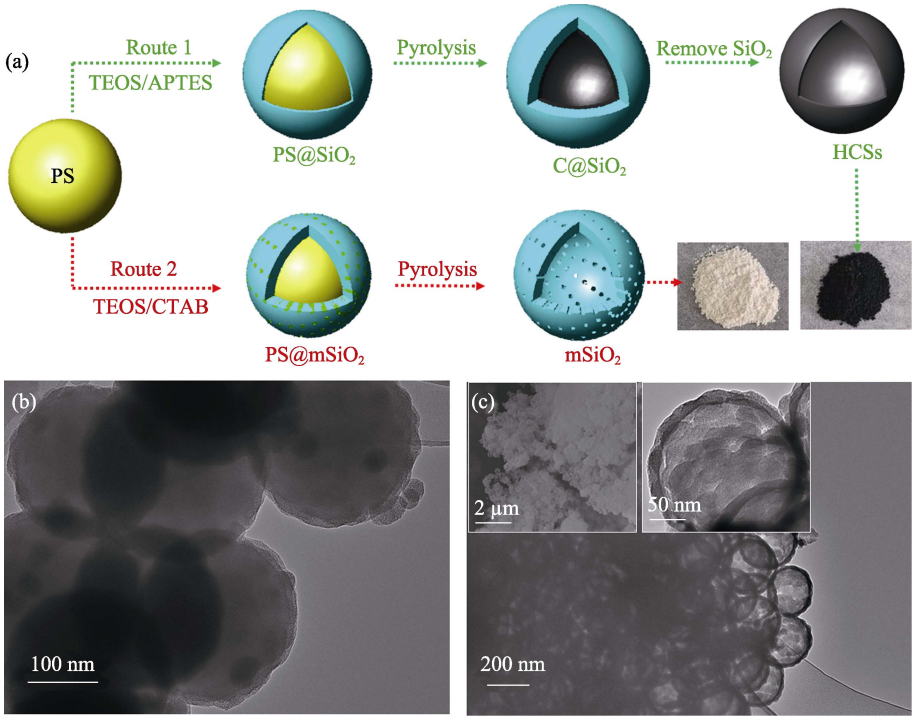


Fig. 1 Preparation routes and TEM (b,c) and SEM (c) images

(a) Schematic illustration of the synthesis of the HCS (Route 1) and hollow mesoporous silica spheres (Route 2); (b) TEM image of PS@m$SiO_2$; (c) TEM and SEM images of m$SiO_2$

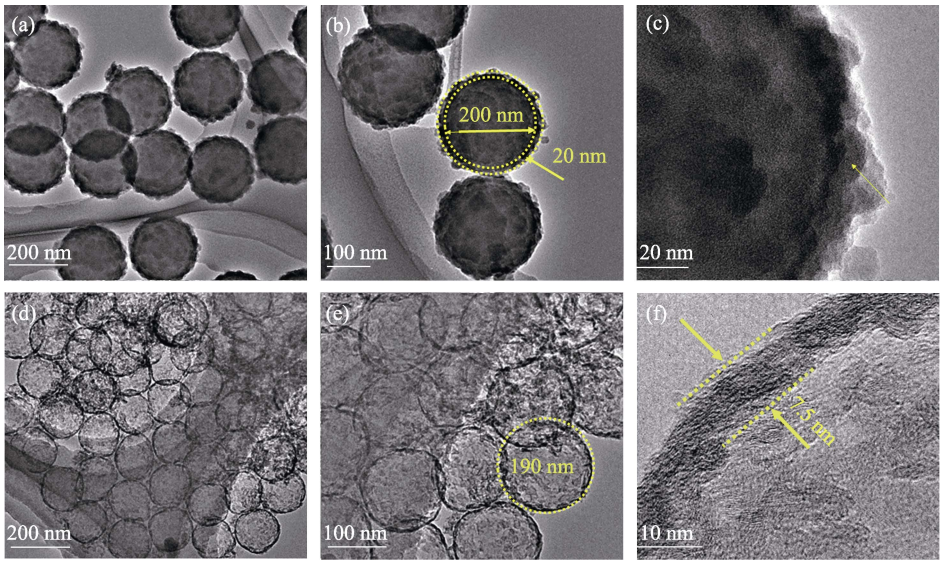


Fig. 2 TEM images of PS@$SiO_2$ hybrids sphere (a-c) and HCS-1 (d-f)

with a thickness of approximate 20 nm seeing from the Fig. 2(b). Moreover, a higher resolution TEM image of PS@$SiO_2$ (Fig. 2(c)) exhibited the PS surface was covered with compact $SiO_2$, providing an enclosed space for the encapsulation pyrolysis of PS. Notably, the surface was crude and there was no obvious pores found (the yellow arrow in Fig. 2(c)), attributing to the deposition of silica oligomer particles.

After deposition of carbon species generated from pyrolysis of the PS and subsequent removal of the compact silica shell, discrete and uniform HCS-1 are produced (Fig. 2(d)). The resulting HCS-1 had a diameter of 190 nm (Fig. 2(c)), which was smaller than that of the PS seed (*ca.* 200 nm), showing the deposition of decomposed PS happened in the inner encapsulation nanoreactor. In addition, the formation of carbon indicated that the shell was enclosed and thus allowed deposition of carbon species generated from pyrolysis of PS. As shown in Fig. 2(f), the high resolution TEM images of HCS-1 showed the thickness of microporous and amorphous carbon shell with size of 7.5 nm, indicating the irregular deposition of carbon species.

The amount of TEOS is very critical on the structure of HCS. Therefore, we tried to synthesize HCS with different thickness of carbon shell through changing the amount of TEOS. As shown in Fig. 3(a), when the amount of TEOS increased from 1 to 1.5 mL, the HCS-1.5 with more uniform spherical structure was obtained. Notably, the diameter of HCS-1.5 was same with HCS-1 (*ca.* 190 nm) (Fig. 3(b)), confirming that the carbon species deposition behavior in the inner compact silica shell. Moreover, the shell thickness increased from 7.5 to 13.5 nm (Fig. 3(c)), showing that larger amount of TEOS would play a better encapsulation effect and more carbon residue left.

In order to further investigate the effect of TEOS amount in this encapsulation pyrolysis, we further reduced the TEOS amount to decrease the shell thickness of HCS. It was clear that the HCS-0.5 possessed mainly spherical morphology with some small fragmentized spheres (the red arrow in Fig. 3(d)). Compared with HCS-1.5, the diameter of HCS-0.5 unchanged and was also *ca.* 190 nm (Fig. 3(e)), which was the same with that of HCS-1 and HCS-1.5. Furthermore, the high-resolution TEM image in Fig. 3(f) clearly showed the thickness of HCS-0.5 at 4.5 nm, thinner than many other carbon shell derived from resin[12-13] and ionic liquids[14]. Additionally, some carbon fragments appeared on the carbon shell (the red arrow in Fig. 3(f)), implying that the thin silica shell could not provide an enough strong encapsulation condition for pyrolysis of PS. By further fitting the thickness of carbon shell *vs* amount of TEOS, a probable liner relationship between two variables was provided in Fig. 3(g). Overall, large amount of TEOS leads to thick shell in HCS. Notably, it could not change the diameter of HCS by changing the amount of TEOS, indicating the deposition occurred inside the silica shell.

The mechanism of encapsulation pyrolysis synchronous deposition strategy was exhibited in Fig. 3(h, i). During pyrolysis of PS, the volatile carbonaceous species would penetrate through the open pore channel (Fig. 3(h)). Conversely, as shown in Fig. 3(i), when the pyrolysis of PS was confined in a compact silica shell, an increase of temperature results in the intrinsic thermal shrinkage of silica and carbon (char) materials, leading to an increase in density of the outer shell[15]. The pressure-tight silica shell could provide an encapsulation nanoreactor for pyrolysis and synchronous deposition of PS. The generated volatile carbonaceous species derived from pyrolysis of PS preferentially stay in the hollow

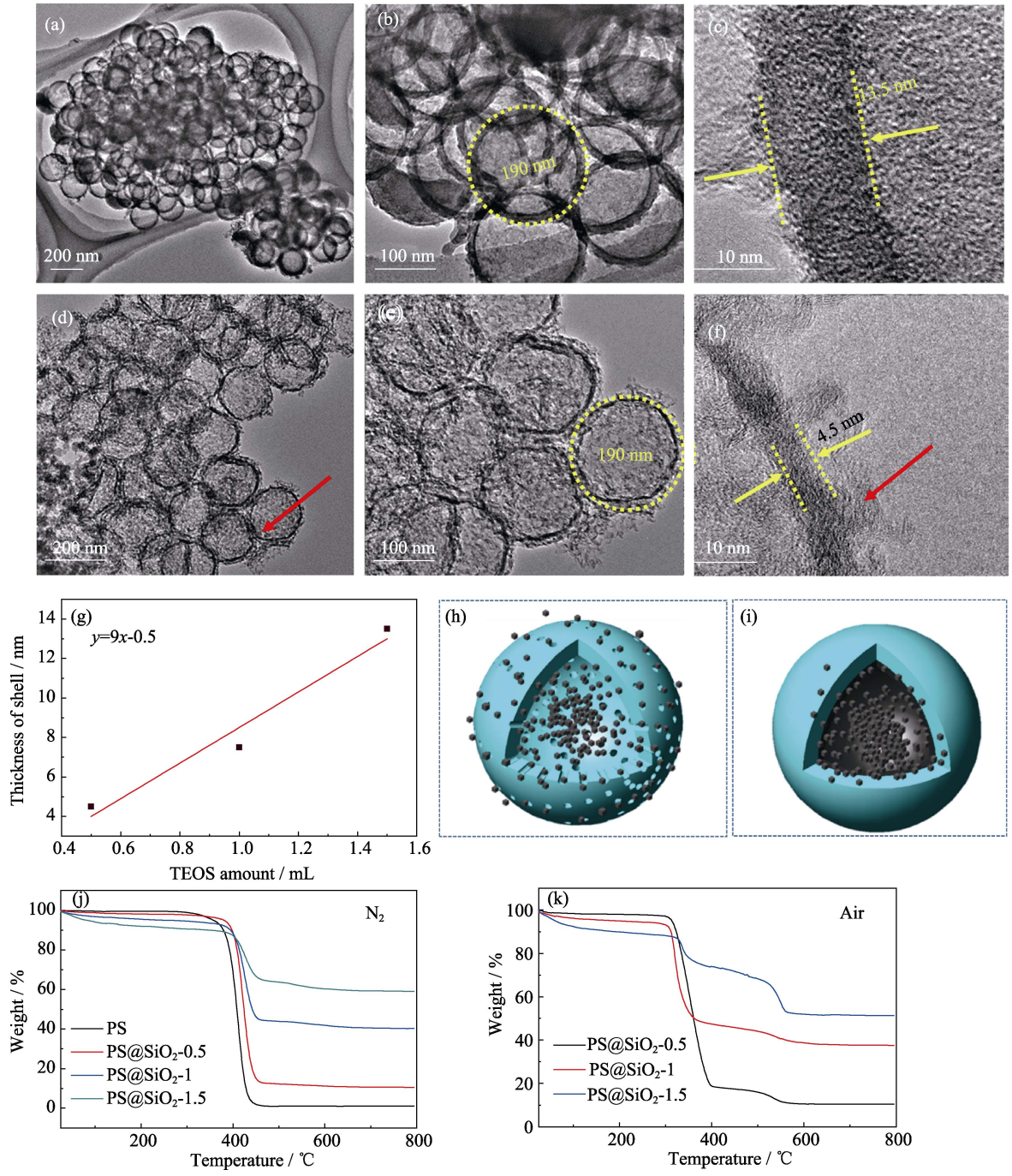


Fig. 3 TEM images of HCS-1.5 (a-c) and HCS-0.5 (d-f), the relationship between TEOS amount and HCS thickness (g), and schematic illustration for the pyrolysis deposition of the PS inside the mesoporous silica shell (h) and the silica shell encapsulation nanoreactor (i), TGA analyses of PS and PS@$SiO_2$ samples in $N_2$ (j) and air (k)

nanospace rather than go out of the hollow nanostructures due to the limiting of compact silica shell. Meanwhile, the thermal expansion force tends to push the carbonaceous gases to deposit on the inner surface of the carbon/silica shell, giving rise to a hollow void[16]. Until the pressure within the hollow space reaches a critical value, the trapped gases can penetrate the silica and carbon shells and go outside. As a consequence, a higher TEOS amount may lead to a thicker silica shell, providing a more solid encapsulation nanoreactor and leading to more carbon residue. On the contrary, when the silica coating on the surface of PS was not enough to provide a condensed solid shell, less carbon residue was remained inside the shell and some carbon fragments were formed on the carbon shell (Fig. 3(i)). Additionally, this assumption of mechanism was further confirmed by Thermogravimetric analysis (TGA) in $N_2$ and air (Fig. 3(j-k)). The PS sphere could completely pyrolysis in $N_2$ (Fig. 3(j)). The carbon residue was 1.0%, 2.7% and 7.9% when the amount of TEOS was 0.5, 1.0 and 1.5 mL, respectively,

based on the calculation of TGA in $N_2$ and air (Fig. 3(j, k)), showing that more TEOS provided favorable condition for deposition of carbon species.

The specific textural properties of HCS were studied by $N_2$ adsorption-desorption isotherm (Fig. 4(a)). $N_2$ adsorption-desorption isotherms of HCS with different thickness all exhibited typical type-IV curves hysteresis[17]. Moreover, the isotherms of three HCS have the same sharp increase in relative pressure range of 0.9–1.0, indicating formation of hollow core during this outer silica assisted deposition. With the decreasing amount of TEOS, the surface areas of HCS-0.5, HCS-1 and HCS-1.5 were 1120, 404 and 245 $m^2 \cdot g^{-1}$, respectively, and the total pore volumes correspondingly decreased from 1.24 to 1.20 and to 0.62 $cm^3 \cdot g^{-1}$. The HCS-0.5 possessed the highest surface area and pore volume which might be attributed to the thin carbon shell and small carbon fragments. The pore-size distributions reveal that HCS-1.5 have no obvious pore-size distribution (Fig. 4(b)). In comparison, HCS-0.5 has a narrow pore-size distribution centered at 4.1 nm, contributing to carbon fragments as seen from TEM. Additionally, there was a wide peak for the pore-size distribution of HCS-1, which might be ascribe to the fully carbon shell. The wide angle X-ray diffraction pattern of HCS-1 could be seen in Fig. 4(c). Two wide characteristic peaks of the HCS-1 was located at around $2\theta = \sim 23°$ and 44° corresponding to the amorphous carbon[18], being well agree with the result of TEM.

X-ray photoelectron spectroscopy (XPS) was performed to further analyze the surface chemical performance of the synthesized HCS-1. As shown in Fig. 4(d), only two peaks were detected in the XPS survey spectra at 284.6 and 532.5 eV, corresponding to C1s, and O1s. There were no other impurities in the HCS-1, indicating the successful deposition of carbon. Quantitative analysis elucidated that the content of C and O was 96.94 and

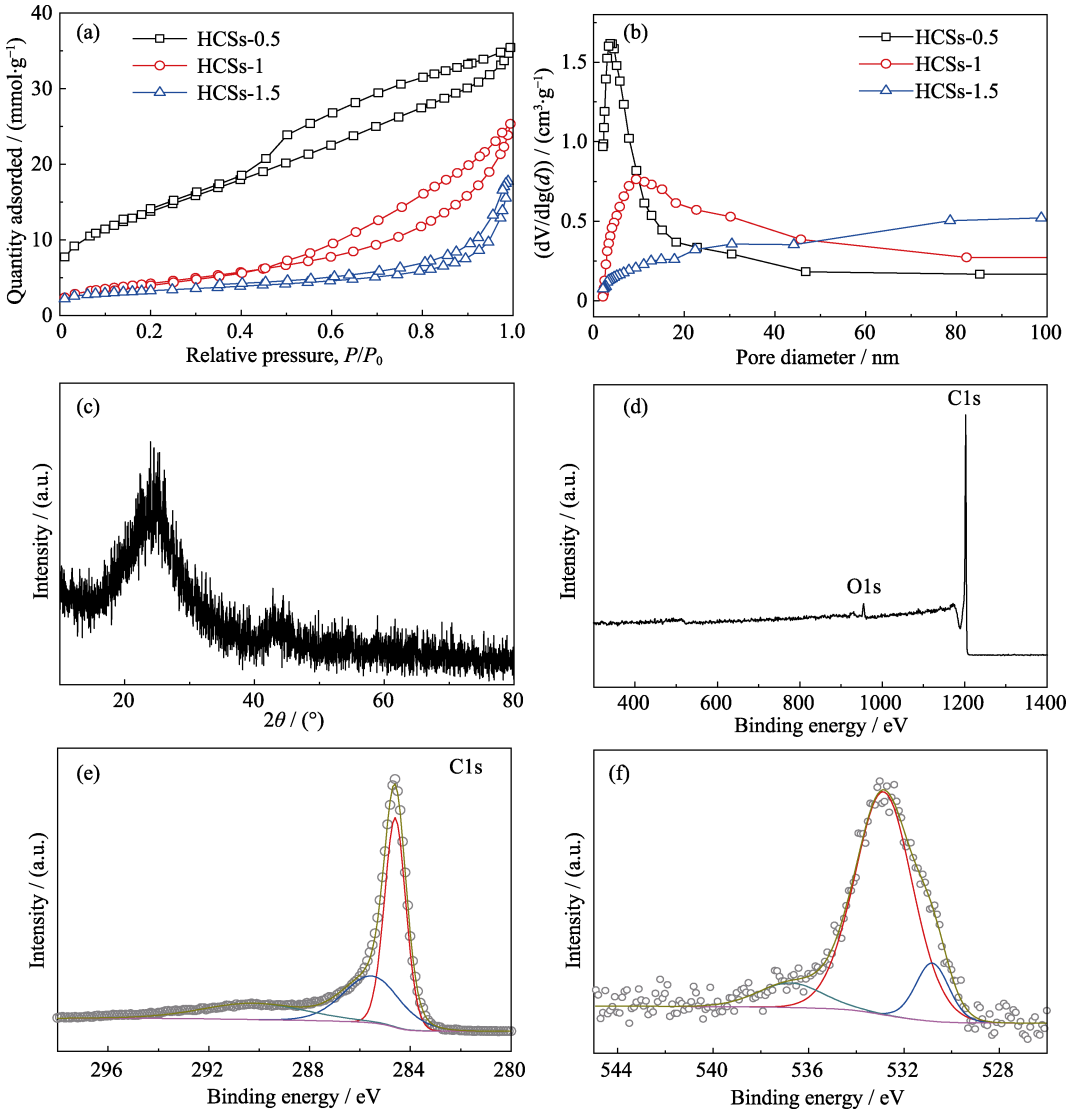


Fig. 4 $N_2$ adsorption-desorption isotherms (a) and pore distributions (b) of HCS, XRD patterns of HCS-1 (c), XPS spectra of HCS-1 (d), C1s (e) and O1s (f) spectra of HCS-1

3.06at%, respectively. The C1s core-level spectrum was divided into three components centering at 284.6, 285.5 and 289.0 eV (Fig. 4(e)), being ascribed to the primary C–C/C=C carbon bonds, residual C–O bonds and C=O bonds formed in the pyrolysis process of PS[19]. As displayed in Fig. 4(f), the XPS O1s spectra of HCS-1 could be deconvoluted into two peaks corresponding to an unsaturated carbonyl group (531 eV) and an ester or anhydride group (533 eV)[20].

Furthermore, the diameter of HCS could be tuned by varying the size of PS spheres. The scanning electron microscopy (SEM) images in Fig. 5(a-c) showed HCS with diameters of 400, 900 and 1600 nm. As shown in Fig. 5(a), the HCS with diameter of 400 nm possessed uniform and complete spherical morphology. However, with the increasing diameter of PS, the obtained HCS became more and more fragmentary, and broken spheres formed on the surface of the hollow carbon spheres after etching of the silica (Fig. 5(b, c), which might be due to the high pressure with larger diameter of PS sphere in the encapsulation nanoreactor. When the diameter of cavity became large, larger amount of volatile carbonaceous species derived from pyrolysis of PS generated. However, the large compact silica shell was unable to withstand the high pressure, resulting in that those volatile carbonaceous species break through the shell and leading to a fragmentized carbon sphere. $N_2$ adsorption-desorption isotherms were also measured to determine the porous structure of the HCS with different diameter (Fig. 5(d)). Three HCS samples presented a typical IV-type curves, indicating the porous and hollow structures. With the increasing of diameter, the BET surface areas decreased to be 502, 404 and 109 $m^2 \cdot g^{-1}$. A wide peak at 20 nm clearly distinguished in the pore size distribution of the HCS (inset in Fig. 5(d)), ascribing to the fragmentary and mesopore formed on the surface of the hollow carbon spheres.

Excessive antibiotic use has caused serious environmental pollution in the world. The high surface-to-volume ratios of the hollow carbon show many advantages in treating antibiotic wastewater. Generally, the cavity of the hollow sphere can provide a space for mass storage, thus improving the adsorption capacity of the material. In addition, the thin shell of the hollow sphere can provide convenience for the rapid transmission of substances. Herein, we selected cefalexin as a typical model drug to study the adsorption performance of HCS. Considering the highest specific surface area and favorable translation of thin shell, the HCS-0.5 was selected as typical absorbent for adsorption of cephalexin. The time-resolved adsorption capacities of cefalexin on HCS-1 were shown in Fig. 6(a). Remarkably, the adsorption capacity of activated HCS-1 was *ca*. 291 $mg \cdot g^{-1}$. Noticeably, the HCS-1 showed high adsorption in short time, attributing to the developed and directly accessible porosity of these nanosized hollow spheres. Fig. 6(b) shows the equilibrium adsorption curves after adsorption for 24 h. The adsorption capacity of HCS-1 increased with increasing

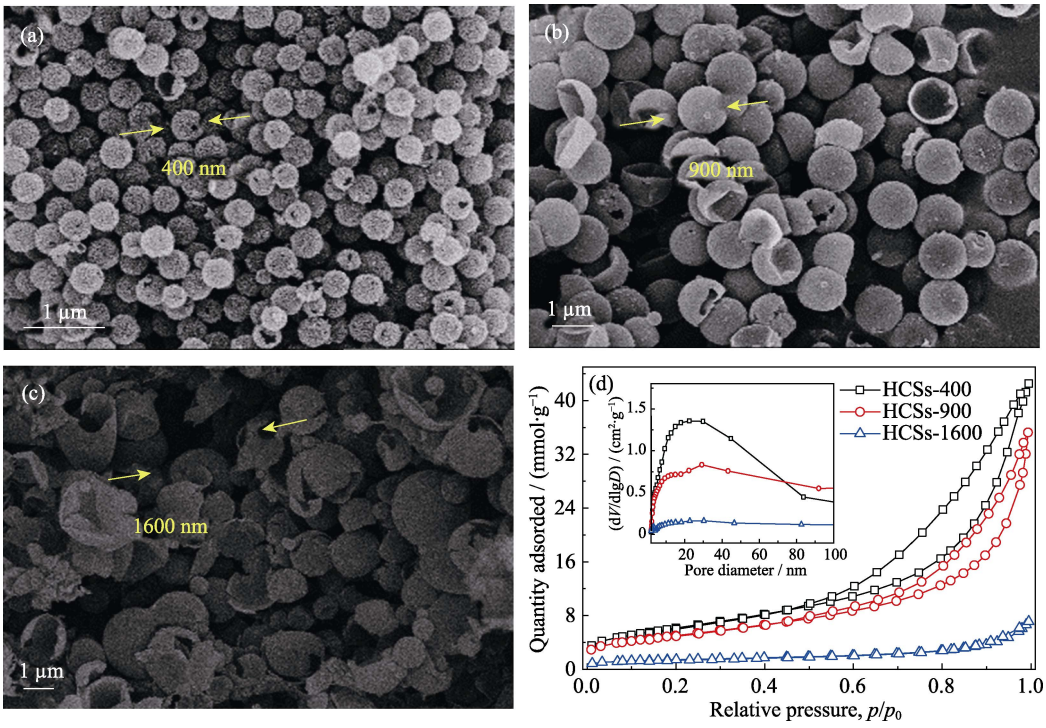


Fig. 5 SEM images of HCS with dimeter size of 400, 900 and 1600 nm obtained by changing the dimeter of PS (a-c) and $N_2$ adsorption-desorption isotherm (d) and pore distribution (inset) of HCS

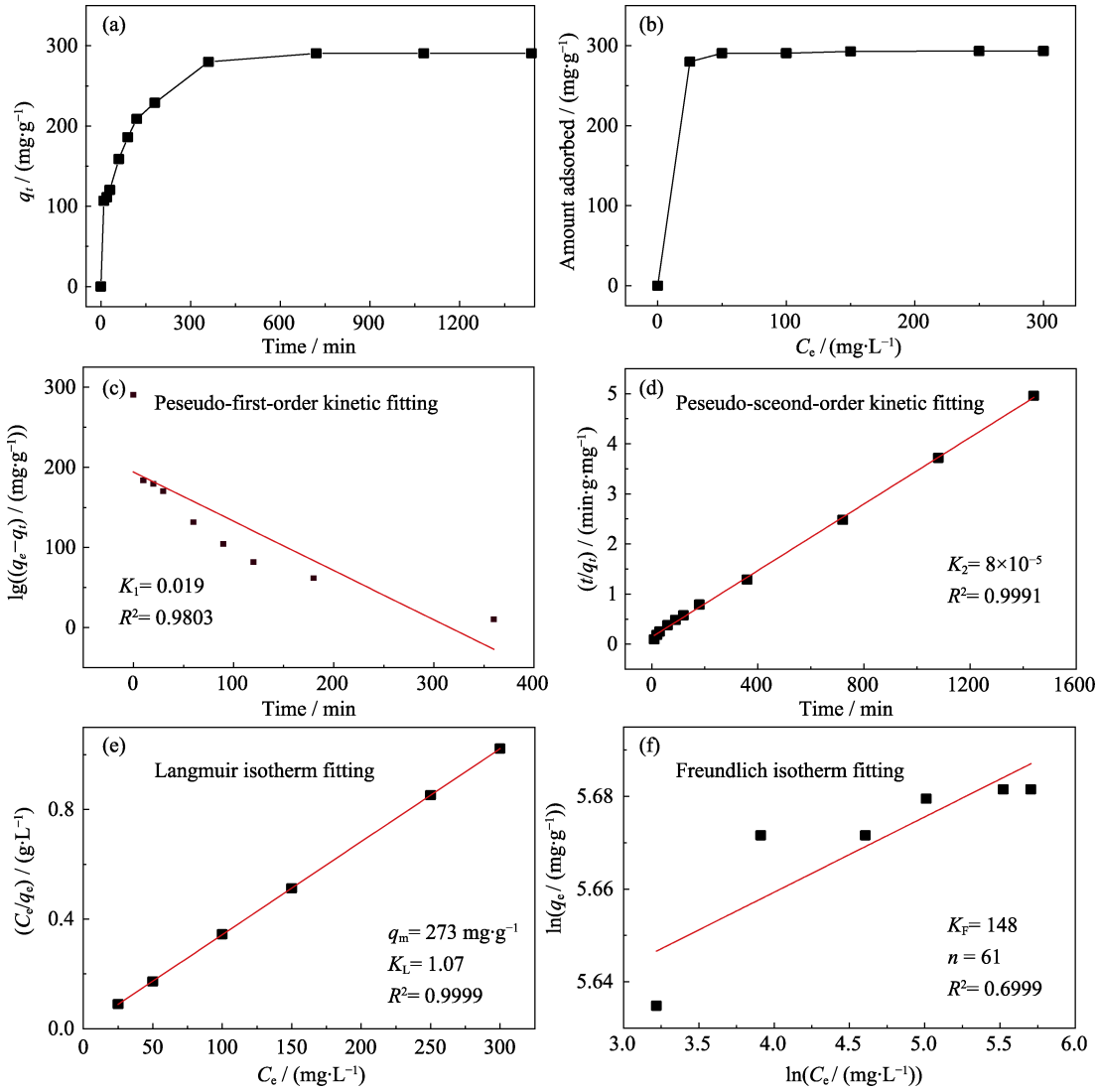


Fig. 6 Adsorption curve of cefalexin over HCS-1 for the contact time (a), various initial concentrations (b), and corresponding Kinetics (c-d) and isothermal (e-f) fittings

equilibrium concentrations. However, cefalexin could no longer be adsorbed with a certain equilibrium concentration and the highest adsorption capacity of HCS-1 for cefalexin was found to be 293 mg·g$^{-1}$, which was higher than that of other carbon materials[21-22], showing the prospect in the treatment of antibiotic wastewater.

The kinetic and isotherm models were also used to elucidate the adsorption process. The pseudo-first-order kinetics and pseudo-second-order kinetics models were used to test the correlation between the adsorption rate and equilibrium time. The adsorption kinetic plots and the predicted kinetic parameters were presented in Fig. 6(c, d). As observed, the pseudo-second-order kinetics model was more suitable for cefalexin adsorption due to its higher regression coefficient ($R^2$=0.9991). The adsorption process was likely to occur on the surface of materials and would last until the surface sites were completely occupied. In addition, the study on adsorption equilibrium was performed for HCS-1. The Freundlich sorption model (Fig. 6(e)), represented by an empirical equation, was not good ($R^2$=0.6999). This indicated that adsorption of cefalexin on HCS-1 was not heterogeneous adsorption. However, the obtained regression coefficient by Langmuir model was 0.9999 (Fig. 6(f)), indicating the adsorption isotherm fitted Langmuir model well. The maximum theoretical adsorption capacity calculated by Langmuir model was 273 mg·g$^{-1}$, which was approximately in close agreement with the measured data, illustrating that the adsorbed cefalexin formed a monolayer coverage on the adsorbent surface and all adsorption sites possessed equal, uniform adsorption energies. Therefore, the pseudo-second-order kinetics and Langmuir isotherms model can well describe the adsorption behavior of HCS-1.

## 3 Conclusion

To summarize, we have demonstrated a novel and efficient encapsulation pyrolysis synchronous deposition

method to prepare HCS with tailorable particle size and well controlled thickness of carbon shell. We confirmed that the encapsulation nanoreactor, made by hermetical silica shell, could successfully provide nanospace for deposition of volatile carbonaceous species derived from pyrolysis of PS. The diameter of HCS and thickness of carbon shell could be tuned by changing the size of PS and amount of TEOS, respectively. The obtained HCS showed uniform spherical morphology with diameter from 200 to 1600 nm and different thickness of carbon shell (4.5−13.5 nm). The HCS exhibited a good performance for treatment of antibiotic waste water. In addition, this encapsulation pyrolysis synchronous deposition strategy may also be applied for the preparation of HCS using other easily decomposing polymer, *e.g.*, polyethylene, polyvinyl alcohol and polyacrylonitrile.

## References:


[1] BIN D S, CHI Z X, LI Y, *et al*. Controlling the compositional chemistry in single nanoparticles for functional hollow carbon nanospheres. *J. Am. Chem. Soc.*, 2017, **139(38):** 13492–13498.

[2] LI D, FENG C, LIU H K, *et al*. Hollow carbon spheres with encapsulated germanium as an anode material for lithium ion batteries. *J. Mater. Chem. A*, 2015, **3(3):** 978–981.

[3] QIAN H, TANG J, HOSSAIN M S A, *et al*. Localization of platinum nanoparticles on inner walls of mesoporous hollow carbon spheres for improvement of electrochemical stability. *Nanoscale*, 2017, **9(42):** 16264–16272.

[4] HOU J, CAO T, IDREES F, *et al*. A co-sol-emulsion-gel synthesis of tunable and uniform hollow carbon nanospheres with interconnected mesoporous shells. *Nanoscale*, 2016, **8(1):** 451–457.

[5] CHEN S, CHENG J, MA L, *et al*. Light-weight 3D Co-N-doping hollow carbon spheres as efficient electrocatalyst for rechargeable zinc-air battery. *Nanoscale*, 2018, **10:** 10412–10419.

[6] LU A H, SUN T, LI W C, *et al*. Synthesis of discrete and dispersible hollow carbon nanospheres with high uniformity by using confined nanospace pyrolysis. *Angew. Chem. Int. Ed.*, 2011, **50(49):** 11765–11768.

[7] CHOI J, KIM W S, HONG S H. Highly stable $SnO_2$-$Fe_2O_3$-C hollow spheres for reversible lithium storage with extremely long cycle life. *Nanoscale*, 2018, **10(9):** 4370–4376.

[8] ZOU C, WU D, LI M, *et al*. Template-free fabrication of hierarchical porous carbon by constructing carbonyl crosslinking bridges between polystyrene chains. *J. Mater. Chem.*, 2010, **20(4):** 731–735.

[9] CHEN A, LI Y, YU Y, *et al*. Synthesis of hollow mesoporous carbon spheres via “dissolution-capture” method for effective phenol adsorption. *Carbon*, 2016, **103:** 157–162.

[10] DU J, LIU L, LIU B, *et al*. Encapsulation pyrolysis synchronous deposition for hollow carbon sphere with tunable textural properties. *Carbon*, 2019, **143:** 467–474.

[11] HU F, YANG H, WANG C, *et al*. Co-N-doped mesoporous carbon hollow spheres as highly efficient electrocatalysts for oxygen reduction reaction *Small*, 2017, **13(3):** 1602507.

[12] FANG X, LIU S, ZANG J, *et al*. Precisely controlled resorcinol-formaldehyde resin coating for fabricating core-shell, hollow, and yolk-shell carbon nanostructures. *Nanoscale*, 2013, **5(15):** 6908–6916.

[13] FENG S, LI W, SHI Q, *et al*. Synthesis of nitrogen-doped hollow carbon nanospheres for $CO_2$ capture. *Chem Commun (Camb)*, 2014, **50(3):** 329–331.

[14] CHEN A, YU Y, LV H, *et al*. Thin-walled, mesoporous and nitrogen-doped hollow carbon spheres using ionic liquids as precursors. *J. Mater. Chem. A*, 2013, **1(4):** 1045–1047.

[15] SUN Q, HE B, ZHANG X-Q, *et al*. Engineering of hollow core-shell interlinked carbon spheres for highly stable lithium-sulfur batteries. *ACS Nano*, 2015, **9(8):** 8504–8513.

[16] SUN Q, LI W C, LU A H. Insight into structure-dependent self-activation mechanism in a confined nanospace of core-shell nanocomposites. *Small*, 2013, **9(12):** 2086–2090.

[17] ZHOU G, KIM N-R, CHUN S-E, *et al*. Highly porous and easy shapeable poly-dopamine derived graphene-coated single walled carbon nanotube aerogels for stretchable wire-type supercapacitors. *Carbon*, 2018, **130:** 137–144.

[18] CHONG J, ZHU X, HUANG W, *et al*. The fabrication of size-tunable nitrogen-doped dual-mesoporous carbon nanospheres with excellent thermal stability via colloidal silica driving co-assembly strategy. *Carbon*, 2018, **126:** 156–164.

[19] ZHANG G, WANG J, QIN B, *et al*. Room-temperature rapid synthesis of metal-free doped carbon materials. *Carbon*, 2017, **115:** 28–33.

[20] LIN Y, FENG Z, YU L, *et al*. Insights into the surface chemistry and electronic properties of $sp^2$ and $sp^3$-hybridized nanocarbon materials for catalysis *Chem. Commun.*, 2017, **53:** 4834–4837.

[21] GAO Y, LI Y, ZHANG L, *et al*. Adsorption and removal of tetracycline antibiotics from aqueous solution by graphene oxide. *J. Colloid Interface Sci.*, 2012, **368(1):** 540–546.

[22] CARABINEIRO S A C, THAVORN-AMORNSRI T, PEREIRA M F R, *et al*. Comparison between activated carbon, carbon xerogel and carbon nanotubes for the adsorption of the antibiotic ciprofloxacin. *Catal. Today*, 2012, **186(1):** 29–34.


# 封装热解同步沉积法制备结构可调的中空碳球及其在头孢氨苄吸附中的应用


杜 娟, 刘 磊, 于奕峰, 张 越, 吕海军, 陈爱兵

(河北科技大学 化学与制药工程学院, 石家庄 050018)



**摘 要:** 本研究报道了一种简便的封装热解同步沉积方法, 并可控地制备了直径和壳厚度可调的中空碳球。该方法通过在密闭的二氧化硅壳中热解和同步沉积过程, 将广泛用作牺牲硬模板的聚苯乙烯球转化为碳。实现了聚苯乙烯在致密的二氧化硅壳中通过热解和沉积过程转化为碳, 无需任何交联剂和催化剂, 减少了操作步骤和降低了生产成本。所获得的中空碳球显示出均匀的球形形态, 具有可调节的颗粒尺寸(190~1600 nm)和良好控制的介孔结构。此外, 通过改变二氧化硅前体的用量, 获得具有精确调节的厚度(4.5~13.5 nm)的碳材料。所得的样品具有头孢氨苄吸附作用, 显示出良好的应用前景。此外, 这种合成策略为碳材料生产提供了一种有效的途径, 有助于其商业应用。



**关 键 词:** 空心碳球; 封装热解同步沉积; 可调结构; 头孢氨苄吸附

**中图分类号:** TQ174 **文献标识码:** A